Modeling and Analysis of Periodic Energy Control for Series–Series Wireless Power Transfer System

Tianlu Ma, *Student Member, IEEE*, C. Q. Jiang, *Senior Member, IEEE*, Yilin Zhang, Yue Wang, *Senior Member, IEEE*, Yuan Cheng, *Member, IEEE*, and Shumei Cui

***Abstract*—Wireless power transfer (WPT) is an emerging technology that enables efficient and convenient transmission of electrical energy wirelessly, and it has gained significant attention due to its potential to revolutionize various industrial, commercial, and consumer applications. This article presents a study on the series-series (SS)-compensated WPT system, focusing on characteristics analysis of periodic energy control (PEC) by the extended describing function (EDF) model. The model incorporates the influence of equivalent series resistors in the transmitting and receiving coils. The research highlights the feature of the PEC's input impedance angle always being greater than zero, which is attributed to the phase limitation of its driving circuit, making it suitable for zero voltage switching operations. In addition, the study reveals that the operating frequency range of PEC is discontinuous and exhibits a piecewise monotonic property against frequency splitting. This research provides valuable insights for the accurate modeling and understanding of PEC behavior in SS-compensated WPT systems. Finally, simulations and experiments are conducted, the EDF model is verified with high accuracy, and the frequency skip is demonstrated. The dc–dc system efficiency is up to 95.3% for the WPT system using PEC.**

***Index Terms*—Extended describing function (EDF), frequency splitting, modeling, periodic energy control (PEC), wireless power transfer (WPT).**

Manuscript received 12 September 2023; revised 21 November 2023; accepted 16 December 2023. Date of publication 25 December 2023; date of current version 16 February 2024. The Work of Yuan Cheng and Shumei Cui was supported in part by the Project of HIT-Hong Kong Exchanges, in part by the Science Technology and Innovation Committee of Shenzhen Municipality, China, under Grant SGDX20210823104003034, in part by the Natural Science Foundation of China, China, under Grant 52107011, in part by Research Grants Council, Hong Kong SAR under ECS Grant 21200622, and in part by the City University of Hong Kong under Grant APRC 9610529. Recommended for publication by Associate Editor J. Biela. *(Corresponding author: C. Q. Jiang.)*

Tianlu Ma and C. Q. Jiang are with the Department of Electrical Engineering and State Key Laboratory of Terahertz and Millimeter Waves, City University of Hong Kong, Hong Kong, China, and also with the City University of Hong Kong Shenzhen Research Institute, Shenzhen 518057, China (e-mail: tianlu.ma@my.cityu.edu.hk; chjiang@cityu.edu.hk).

Yilin Zhang is with the Sustainable Energy and Environment Thrust, Function Hub, and Power Electronics Exploration Research Lab, Hong Kong University of Science and Technology (Guangzhou), Guangzhou 511400, China (e-mail: yilinzhang@hkust-gz.edu.cn).

Yue Wang is with the School of Electrical Engineering and the State Key Laboratory of Electrical Insulation and Power Equipment, Xi'an Jiaotong University, Xi'an 710049, China (e-mail: davidwangyue@mail.xjtu.edu.cn).

Yuan Cheng and Shumei Cui are with the School of Electrical Engineering and Automation, Harbin Institute of Technology, Harbin 150001, China, and also with the Chongqing Research Institute, Harbin Institute of Technology, Chongqing 401135, China (e-mail: chengyuan@hit.edu.cn; cuism@hit.edu.cn).

Color versions of one or more figures in this article are available at https://doi.org/10.1109/TPEL.2023.3346460.

Digital Object Identifier 10.1109/TPEL.2023.3346460

I. Introduction

WIRELESS power transfer (WPT) is an effective, popular, safe, flexible, and convenient technology for many devices, like electric vehicles [1], drones [2], and underwater robots [3]. It is an attractive alternative to traditional wired charging methods. However, to ensure optimal performance and safety of WPT systems, it is essential to develop effective control strategies and accurate models that can accurately predict and regulate the power transfer process. These control strategies and models play a crucial role in enabling efficient power transfer, minimizing power losses, and ensuring system stability.

The control strategies will be applied to the controllable parts of the WPT system, such as the inverter, rectifier, and dc–dc converters on the primary or secondary sides. The inverter transfers the dc voltage into ac voltage, and its operating frequency is close to the nominal resonant frequency of resonant tanks on the primary and secondary sides. Variable frequency control (VFC) manages the switching frequency of the inverter, thus regulating the system output because the voltage gain and the switching frequency are related [4]. Nevertheless, the reactive power can degrade the system efficiency when there is a big deviation between the switching frequency and nominal resonant frequency. Furthermore, phase-shifted modulation can be utilized to adjust the phase-shifted angle between the front and rear bridge arms of the full bridge inverter [5]. The root mean square value of the inverter's output voltage diminishes with the enlargement of the phase-shifted angle. Although phase-shifted modulation can realize a low reactive power by fixing an optimal frequency, zero-voltage-switching (ZVS) will vanish with a light load condition. Pulse density modulation controls the system output by adjusting the density of driving signals, which will excite harmonics [6], [7]. Meanwhile, the fluctuation of current and voltage also threatens the ZVS. Model predictive control has a fast dynamic response, which relies on the high-accuracy mathematical model [8], [9], [10]. System trajectory can be predicted by the model, and the optimal control variables can be solved by the optimization algorithm. Nonetheless, the huge computational burden limits its application in high-frequency conditions, which means less computing time.

On the other hand, the rectifier transfers the dc voltage into ac voltage on the secondary side. Active or semiactive rectifiers can regulate the output voltage by controllable semiconductors [11]. In addition, dc–dc converters can be added on the primary and secondary sides to regulate the voltage and impedance [12]. Certainly, the controllable parts on the primary or secondary

sides can be combined to achieve better performance. For instance, the triple-phase-shift strategy is used to realize maximum efficiency tracking during a wide output voltage range in [13], where the phase-shifted angle between the front and rear arms of the inverter and rectifier and the phase-shifted angle between the output voltage of the inverter and rectifier are all regulated.

Mathematical modeling plays a crucial role in power electronics, which allows engineers to design and analyze systems before prototype development. Also, it can describe system trajectory and aid in optimizing system efficiency, reliability, and stability. Fundamental harmonic approximation (FHA) is an effective modeling method because fundamental harmonic constitutes the predominant element in the WPT system [14], [15]. Nevertheless, the presence of higher order harmonics exhibits an escalating trend for WPT systems with wide-load and wide-coupling characteristics. The complex Laplace transformation is an effective tool that transforms a function of time into a function of a complex variable, whereas system initial conditions need to be considered [16]. The generalized state-space averaging (GSSA) approach provides a way to model power electronic converters as time-independent systems, i.e., approximating the state variables of the circuit using a Fourier series expansion [17], and it is suitable for the WPT system [18]. Different from GSSA, the extended describing function (EDF) method expresses each state variable in trigonometric form instead of exponential form [19], and each state variable can be separated by sine, cosine, or dc terms. In fact, the sine or cosine terms correspond to the value of state variables at two different moments. Therefore, the EDF method can be utilized to build the model for the system where the control variable is related to sine or cosine terms of any state variables. FHA, GSSA, and EDF methods can be easily extended and obtain a higher accuracy by considering high-order harmonics. For example, harmonic modeling was built in [20] and [21], which is regarded as the extension of FHA. Nevertheless, there is no doubt that multiple harmonics will lead to an exponential increase in computational complexity, and the gyrator model can be used to simplify complex circuits by replacing inductors or coupling coils with gyrators, thus decreasing the order of the model [22], [23].

The time-domain modeling method usually has a higher accuracy than the ones in the frequency domain, thanks to not ignoring high-frequency harmonics. The sampled-data model of the series series (SS)-compensated WPT system was established in [24], and its accuracy was proven to be higher than the GSSA model. Similarly, the discrete-time model was successfully applied to multiple compensation networks of WPT systems to solve problems. For instance, the stability of the LCC-S compensated WPT system was analyzed, and controller parameters were optimized in [25]. Also, efficiency optimization was conducted for the LCC–LCC compensated bidirectional WPT system using a discrete-time model in [26]. In addition, the unified full-load discrete-time model, which is a form of the extension of the discrete-time model, was derived to analyze the discontinuous conduction of the passive rectifier [27]. Moreover, time-domain analysis can also be utilized to identify the zones of continuous or discontinuous conductions of the passive rectifier [28], and it has an analytical solution but with a complex result. The mathematical model is an effective tool for analyzing the system characteristics and optimizing the performance of control strategies. It is important to select a suitable model for analysis.

Periodic energy control (PEC) is a new control strategy that adjusts energy flowing into the resonant network, which is quite different from traditional control methods. It was first proposed in [29], and compared with VFC because the working frequency of PEC is changed for different references. PEC has been proven to have a better performance than VFC in terms of dynamic response and overshoot suppression by experiments but without deep explanation in the mathematical model, and many unique phenomena still need to be explained. Therefore, the mathematical model of PEC is established to reveal its working mechanisms and to analyze its characteristics. Although the order of the EDF model is relatively high, it is still selected to model for PEC and analyze the characteristics of PEC because the control variable of PEC is a state variable of the EDF model. The contributions are listed as follows.

1) The accurate EDF model of PEC in the SS-compensated WPT system is derived considering the equivalent series resistors (ESRs) of transmitting and receiving coils.
2) The feature that the input impedance angle of PEC is always larger than zero is achieved due to the phase limitation of its driving circuit, which is friendly for ZVS.
3) The operating frequency range of PEC is proven to be discontinuous, and PEC follows a piecewise monotonic property against frequency splitting with a large coupling coefficient.

The rest of this article is organized as follows. In Section II, the structure and mechanism of PEC for SS-compensated WPT systems are introduced. In Section III, the large signal model and small signal model are derived by EDF. In Section IV, the characteristics are analyzed based on the established model with different load and coupling coefficients. In Section V, the simulations and experiments are carried out to verify the model and features of PEC. Finally, Section VI concludes this article.

II. PEC for SS Compensated WPT Systems

The SS compensation network is widely used in WPT systems due to its simple structure, and its circuit topology and main waveforms are shown in Fig. 1. S_1–S_4 are four semiconductor devices composed of a full-bridge inverter, and D_1–D_4 are four diodes consisting of a full-bridge rectifier. L_1 and L_2 are the self-inductance of transmitting and receiving coils, and their ESRs are expressed as R_1 and R_2. C_1 and C_2 are the compensation capacitors on the primary and secondary sides to compensate for the reactive power, C_f is the filter capacitor, R_f is its ESR, and R_L is the load resistor. M is the mutual inductance between the transmitting and receiving coils, and the coupling coefficient is expressed as

$$k = \frac{M}{\sqrt{L_1 L_2}}. \tag{1}$$

In addition, the voltages and currents are expressed by the symbols u and i with different subscripts.

PEC is a new control method, and it has been applied to the different compensation networks of WPT systems. The principle of PEC is reviewed first. The energy out of the inverter is regulated to manage the system output, and the energy out of

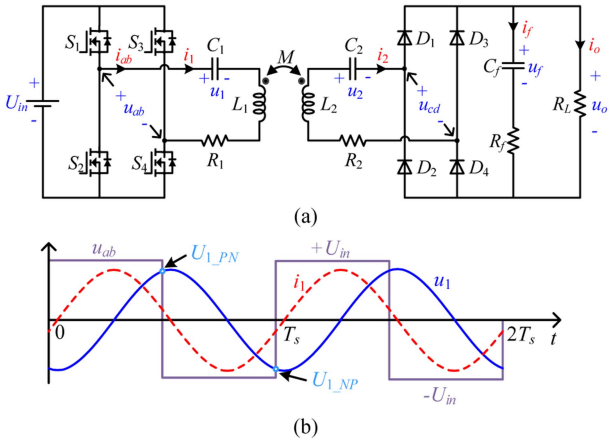

Fig. 1. Overall diagram of the SS-compensated WPT system. (a) Typical circuit topology. (b) Main waveforms on the primary side.

the inverter is simplified based on the compensation networks of WPT systems, which has been summarized in [29] according to two kinds of source types. As for the SS-compensated WPT system, the energy out of the inverter in each switching period can be calculated by

$$E_{ab} = \int_0^{T_s} u_{ab}(t)\, i_{ab}(t)\, dt \tag{2}$$

where u_{ab} and i_{ab} are the output voltage and current of the inverter, and T_s is the switching period. Based on the circuit topology, the current out of the inverter also charges for the capacitor C_1, i.e.,

$$i_{ab}(t) = i_1(t) = C_1 \frac{du_1(t)}{dt}. \tag{3}$$

Assume the input voltage of the SS-compensated WPT system U_{in} is constant in each switching period. Thus, the output voltage of the inverter u_{ab} is equal to + U_{in} and - U_{in} in each half switching period. As a result, the energy calculation can be simplified as

$$\begin{aligned} E_{ab} &= U_{\text{in}} \int_0^{T_s/2} C_1 \frac{du_1(t)}{dt} dt - U_{\text{in}} \int_{T_s/2}^{T_s} C_1 \frac{du_1(t)}{dt} dt \\ &= U_{\text{in}} C_1 \left(\int_{u_1(0)}^{u_1(T_s/2)} du_1 - \int_{u_1(T_s/2)}^{u_1(T_s)} du_1 \right) \\ &= 2U_{\text{in}} C_1 \left(U_{1\_PN} - U_{1\_NP} \right) \end{aligned} \tag{4}$$

where U_{1_PN} and U_{1_NP} are the values of the voltage u_1 at the moments when the output voltage of the inverter u_{ab} switches from positive to negative and switches from negative to positive, as shown in Fig. 1(b). Therefore, capacitor voltage u_1 will be sampled and applied to control the system output for PEC in SS-compensated WPT systems.

III. Modeling for PEC

Extending describing function (EDF) has been used to establish the model of SS-compensated WPT systems in [19]. A T-equivalent model is applied to analyze the coupling coils of the

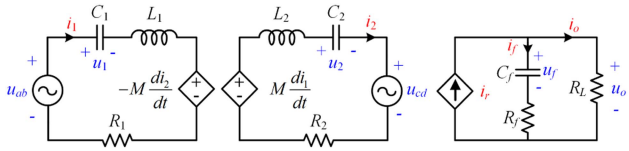

Fig. 2. Equivalent circuit of the SS-compensated WPT system.

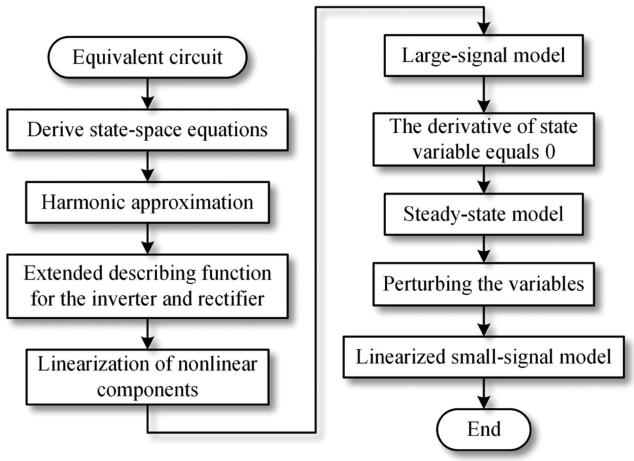

Fig. 3. Flowchart of modeling for WPT systems by the EDF method.

WPT system. Only three traditional control methods, i.e., input voltage control, phase-shifted control, and frequency control, are considered. However, the ESRs of the coils are ignored, which will degrade the accuracy of the model. In this section, the EDF method is utilized to build the mathematical model of PEC. The reason for using the EDF model is that the cosine term, which is one of the state variables, is the control variable of PEC for the SS-compensated WPT system.

A. State Space Equations

The equivalent circuit of the SS-compensated WPT system is shown in Fig. 2, where the directions of the voltage and current are marked. The coupling model is applied for coils rather than the T-equivalent model in [19]. Thus, fewer variables are needed in the model. The state equations can be listed as

$$\begin{cases} u_{ab}(t) = u_1(t) + L_1 \frac{di_1(t)}{dt} - M \frac{di_2(t)}{dt} + i_1(t) R_1 \\ M \frac{di_1(t)}{dt} = L_2 \frac{di_2(t)}{dt} + u_2(t) + u_{cd}(t) + i_2(t) R_2 \\ u_o(t) = u_f(t) + i_f(t) R_f \\ i_1(t) = C_1 \frac{du_1(t)}{dt} \\ i_2(t) = C_2 \frac{du_2(t)}{dt} \\ i_f(t) = C_f \frac{du_f(t)}{dt} \\ i_r(t) = |i_2(t)| = i_f(t) + i_o(t). \end{cases} \tag{5}$$

B. EDF Model of the SS-Compensated WPT System

The modeling process is illustrated by a flowchart in Fig. 3, which has been detailed in [19], and the differences and highlights will be described in this section. The WPT system operation frequency is around the resonant frequency, the fundamental

harmonic is the major item in the whole system, and the current and voltage shape is like a pure sine wave. Therefore, all variables in (5) can be expressed as

$$x(t) = A(t)\sin(\omega_s t + \theta) \tag{6}$$

where $A(t)$ is the amplitude, ω_s is the switching angular frequency, and θ is the phase. According to Ptolemy's identities, (6) can be expanded into

$$x = A(t)\cos(\theta)\sin(\omega_s t) + A(t)\sin(\theta)\cos(\omega_s t). \tag{7}$$

Therefore, variables can be expressed by the sum of the sine item and cosine item, i.e.,

$$x(t) = x_s(t)\sin(\omega_s t) + x_c(t)\cos(\omega_s t) \tag{8}$$

where $x_s(t)$ and $x_c(t)$ are the amplitudes of sine and cosine items. The derivative of the state variable is

$$\begin{aligned}\frac{dx(t)}{dt} = &\left(\frac{dx_{\rm s}(t)}{dt} - \omega_{\rm s}\cdot x_{\rm c}(t)\right)\cdot\sin(\omega_{\rm s}t)\\ &+\left(\frac{dx_{\rm c}(t)}{dt} + \omega_{\rm s}\cdot x_{\rm s}(t)\right)\cdot\cos(\omega_{\rm s}t).\end{aligned} \tag{9}$$

The inverter and rectifier are two nonlinear structures, and their voltages are shaped as a square wave. Apply the Fourier transform, and only fundamental harmonic is considered. The output voltage of the inverter is expressed as

$$u_{ab}(t) = \frac{4U_{in}}{\pi}\sin(\omega_s t). \tag{10}$$

The phase of u_{ab} is the reference phase, and it equals 0. As for the voltage of the rectifier u_{cd}, the fundamental harmonic of the voltage of the rectifier is the same as the current i_2. Therefore, u_{cd} can be expressed as

$$\begin{aligned}u_{cd}(t) &= \frac{4u_o}{\pi}\sin(\omega_s t + \theta_{i2})\\ &= \frac{4u_o}{\pi}\left[\cos(\theta_{i2})\sin(\omega_s t) + \sin(\theta_{i2})\cos(\omega_s t)\right]\end{aligned} \tag{11}$$

where θ_{i2} is the phase of current i_2. The current i_2 can be expressed as

$$\begin{aligned}i_2(t) &= i_{2pk}(t)\sin(\omega_s t + \theta_{i2})\\ &= i_{2s}(t)\sin(\omega_s t) + i_{2c}(t)\cos(\omega_s t)\end{aligned} \tag{12}$$

where i_{2s} and i_{2c} are the amplitude of the sine and cosine term of i_2, i_{2pk} is the amplitude of i_2, and

$$\begin{cases} i_{2pk}^2 = i_{2s}^2 + i_{2c}^2\\ \cos(\theta_{i2}) = i_{2s}/i_{2pk}\\ \sin(\theta_{i2}) = i_{2c}/i_{2pk}.\end{cases} \tag{13}$$

Plug (13) into (11), and u_{cd} can be derived as

$$u_{cd} = \frac{4}{\pi}\frac{i_{2s}u_o}{i_{2pk}}\sin(\omega_s t) + \frac{4}{\pi}\frac{i_{2c}u_o}{i_{2pk}}\cos(\omega_s t). \tag{14}$$

The output current of the rectifier is a dc term, and its average value can be expressed as

$$i_r = \frac{2}{\pi}i_{2pk}. \tag{15}$$

The nonlinear items have been linearized successfully. Plug (8)–(15) into (5), the state equation will be expanded and composed of sine items, cosine items, and dc items. The large signal model can be obtained, and the steady state operating point can also be derived when the derivative of the state variable equals 0, i.e.,

$$X_{\rm ss} = A_{\rm ss}^{-1}B_{\rm ss} \tag{16}$$

where

$$X_{\rm ss} = [U_{1s}, U_{2s}, I_{1s}, I_{2s}, U_{1c}, U_{2c}, I_{1c}, I_{2c}]^T \tag{17}$$

and matrix $A_{\rm ss}$ and $B_{\rm ss}$ are shown in Appendix. The control variables U_{1_PN} and U_{1_NP} are the values of capacitor voltage u_1 at which the phase is π and 0, respectively, i.e.,

$$\begin{cases} U_{1\_PN} = U_{1s}\sin(\pi) + U_{1c}\cos(\pi) = -U_{1c}\\ U_{1\_NP} = U_{1s}\sin(0) + U_{1c}\cos(0) = U_{1c}.\end{cases} \tag{18}$$

The amplitude of U_{1_PN} and U_{1_NP} is defined as U_{th}. The relationship between control variables and other parameters of PEC can be analyzed by the steady state model.

In addition, the small signal model can be obtained by perturbing the state variables around the steady-state operating point, i.e.,

$$x = X + \hat{x}. \tag{19}$$

To solve the small signal model of PEC, the small signal model of VFC will be described first as follows [19]:

$$\begin{cases}\frac{d\hat{x}(t)}{dt} = A\hat{x} + B\hat{\omega}_s\\ \hat{u}_o = C\hat{x}\end{cases} \tag{20}$$

where

$$\hat{x} = [\hat{i}_{1s}, \hat{i}_{1c}, \hat{i}_{2s}, \hat{i}_{2c}, \hat{u}_{1s}, \hat{u}_{1c}, \hat{u}_{2s}, \hat{u}_{2c}, \hat{u}_f]^T \tag{21}$$

and matrices A, B, and C are shown in Appendix. Thus, the transfer function of VFC, switching frequency to output voltage, is derived as

$$H_f(s) = \frac{\hat{u}_o}{\hat{\omega}_s} = C(sI - A)^{-1}B. \tag{22}$$

Then, the control variable of PEC is related to the state variables of the system, as shown in (18), and it can be expressed by

$$U_{th} = C_u x \tag{23}$$

where

$$C_u = [0, 0, 0, 0, 0, -1, 0, 0, 0]. \tag{24}$$

Therefore, the transfer function from switching frequency to threshold voltage can be derived as

$$H_u(s) = \frac{\hat{U}_{th}}{\hat{\omega}_s} = C_u(sI - A)^{-1}B. \tag{25}$$

The transfer function of PEC, threshold voltage to output voltage, can be derived by combining (22) and (25)

$$H_p(s) = \frac{\hat{u}_o}{\hat{U}_{th}} = \frac{H_f(s)}{H_u(s)} = \frac{C(sI - A)^{-1}B}{C_u(sI - A)^{-1}B}. \tag{26}$$

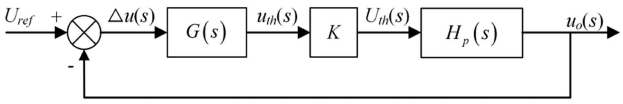

Fig. 4. Control block diagram for PEC with a closed loop.

As a result, the small signal model of PEC is derived cleverly by utilizing the transfer function from switching frequency to threshold voltage, which relies on the fact that the control variable of PEC is one of the state variables. After deriving the small-signal transfer function of PEC, $H_p(s)$, the performance of the closed-loop system can be optimized by designing the controller, $G(s)$, as shown in Fig. 4, where K is a constant determined by the sampling and conditioning circuit. The system's open loop gain is $G(s)*K*H_p(s)$. The energy out of the inverter is the control variable of PEC, and it is reflected by the threshold voltage U_{th} for the SS-compensated WPT system, which has been analyzed in Section II. Therefore, the controller will regulate the threshold voltage and thus manage the system output.

IV. Characteristic Analysis of PEC

The EDF model has been established in the last section, and the characteristics of PEC in SS-compensated WPT systems will be analyzed based on the established model in this section. Two conditions of WPT systems with a small and large coupling coefficient will be discussed because the frequency splitting phenomenon exists for the SS-compensated WPT system with a large coupling coefficient [30], like automated guided vehicles where the distance between the primary and secondary coils is small [31]. The voltage gain and input impedance of the SS-compensated WPT system can be derived based on the large signal model, i.e.,

$$G_v = \frac{u_o}{U_{\text{in}}} \tag{27}$$

$$\begin{cases} |Z_{\text{in}}| = \frac{|u_{ab}|}{|i_1|} = \frac{4U_{\text{in}}/\pi}{\sqrt{I_{1s}^2+I_{1c}^2}} \\ \angle Z_{\text{in}} = \theta_{uab} - \theta_{i1} = -\theta_{i1} = -\arcsin\left(\frac{I_{1s}}{\sqrt{I_{1s}^2+I_{1c}^2}}\right) \end{cases} \tag{28}$$

where $I_{1\,s}$ and $I_{1\,c}$ are the amplitudes of the sine term and cosine term of the current I_1, and the curves of the voltage gain and input impedance with different coupling coefficients are shown in Figs. 5 and 6, where f_n is the normalized switching frequency, i.e., $f_n = f_s/f_0$. It can be found that double peaks occur in voltage gain and three crossover frequencies with zero in the curve of the angle of the input impedance when the coupling coefficient increases.

A. ZVS Operation

The ZVS requires the phase of the output current of the inverter to lag one of the output voltages of the inverter [13], i.e., the angle of the input impedance is larger than 0. It can be noted that the angle of the input impedance varies from $-90°$ to $+90°$ when the switching frequency deviates from the nominal resonant frequency. Nevertheless, PEC can keep the angle of the input impedance larger than 0, and it is important for the

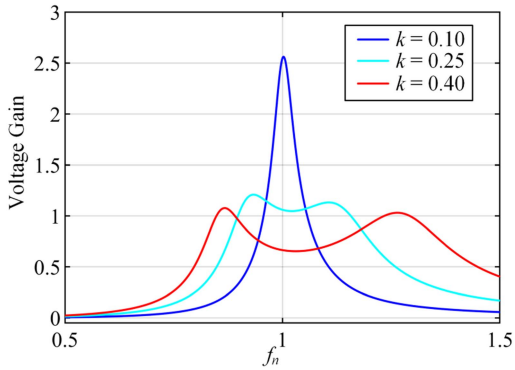

Fig. 5. Voltage gain of the SS-compensated WPT system, $R_L = 10\ \Omega$.

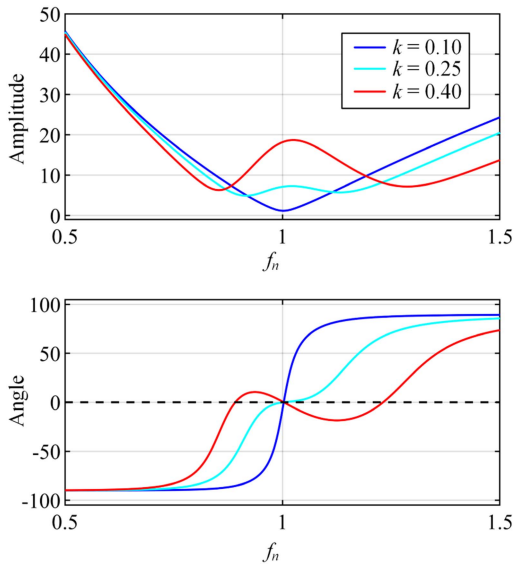

Fig. 6. Input impedance of the SS-compensated WPT system, $R_L = 10\ \Omega$.

characteristics analysis in the following parts. This feature is given by the driving circuit, and the reason is as follows.

The main structure of driving circuit is shown in Fig. 7(a). $u_{1\,att}$ is the signal after capacitor voltage u_1 has been attenuated and lifted, and it is a sine wave with a dc bias voltage of 1.5 V. u_{thH} and u_{thL} are two dc signals and generated by DACs of the digital controller, and they correspond to U_{1_PN} and U_{1_NP} in (4), respectively, whose values reflect the energy out of the inverter and determine the system output. After two comparators, two pulses appear, and then the cascaded RS flip–flop will generate the driving signal of four switches S_1–S_4. Fig. 7(b) illustrates the relationship between main waveforms. Between points A and B, $u_{1\,att}$ is larger than u_{thH}, and the output of comparator 2 is positive. Similarly, the output of comparator 1 is positive between points C and D. Through RS flip–flop, the driving signals of S_2 and S_3 are positive between points A and C, and S_1 and S_4 are activated in the other half switching period (between point C and A'). α is the phase difference between point C and the peak point of current i_1. It should be noted that u_{thL} should be larger than the minimum value of $u_{1\,att}$, and u_{thH} should be smaller than the maximum value of $u_{1\,att}$. Otherwise,

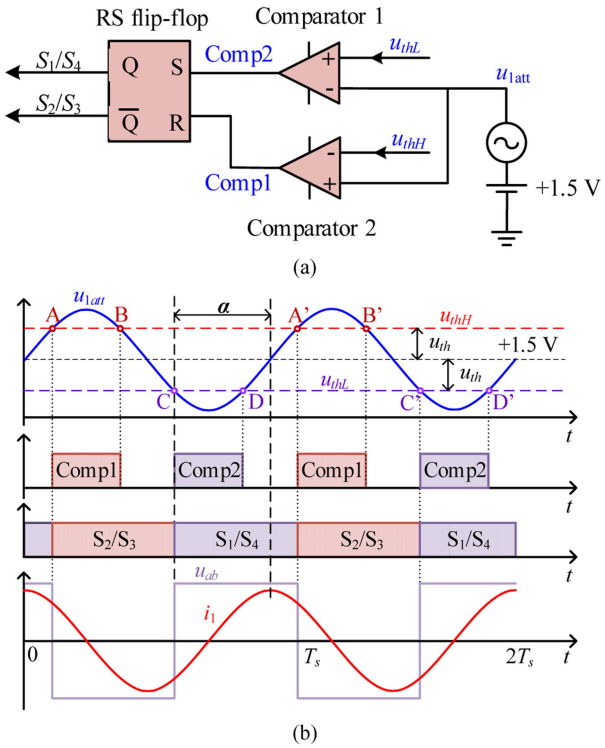

Fig. 7. Control scheme of PEC. (a) Main control structure. (b) Main waveforms.

the system will shut down. Point C is on the left of the minimum value of $u_{1\,att}$, i.e., $\alpha \geq 90°$, which means the phase of current i_1 lags the phase of u_{ab}. Therefore, the driving circuit determines PEC meets the ZVS conditions.

B. Piecewise Monotonic Feature

The input impedance angles vary continuously from $-90°$ to $+90°$ when the normalized frequency increases from 0.5 to 1.5, as shown in Fig. 6(b). Furthermore, the driving circuit determines the angle of the input impedance must be larger than 0, which is explained in Section IV-A. Therefore, the system using PEC works at the segmented frequency range where the input impedance angle is larger than 0. The large signal model is utilized to illustrate the relationship of multiple parameters, and small and large coupling coefficients will be discussed to illustrate the monotonous feature of PEC.

1) Without Frequency Splitting: When the coupling coefficient is small, there is only one peak for voltage gain of the SS-compensated WPT system and one point where the input impedance angle is 0, as shown in Figs. 5 and 6, which means no frequency splitting. Meanwhile, the voltage gain approaches the maximum value while the input impedance angle is 0. Three parameters, including input impedance, voltage gain, and normalized threshold voltage u_{thn}, are calculated by the EDF model, and they are drawn in one polar plot, as shown in Fig. 8. The normalized threshold is defined as

$$u_{thn} = \frac{U_{th}}{\max\left(U_{th}\right)}. \tag{29}$$

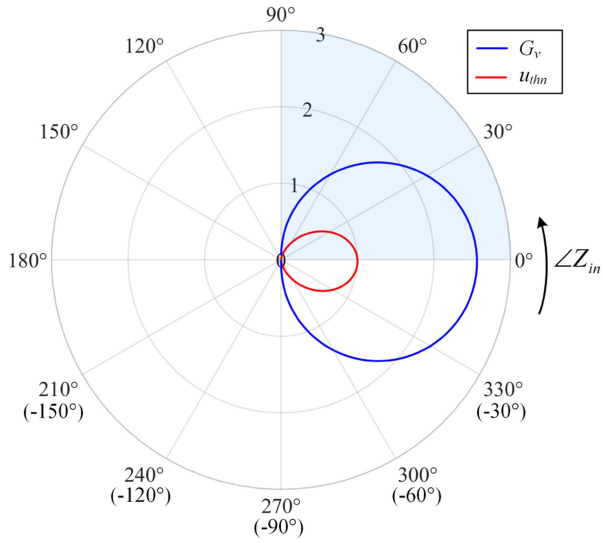

Fig. 8. Polar plot of input impedance angle versus voltage gain G_v and normalized threshold voltage u_{thn}, $k = 0.1$.

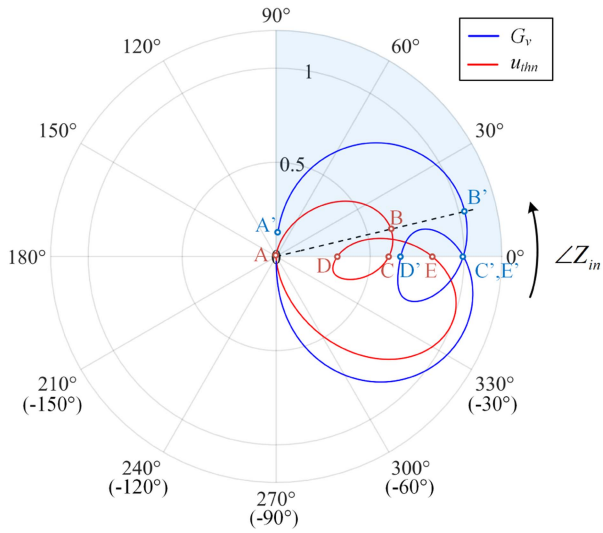

Fig. 9. Polar plot of input impedance angle versus voltage gain G_v and normalized threshold voltage u_{thn}, $k = 0.4$.

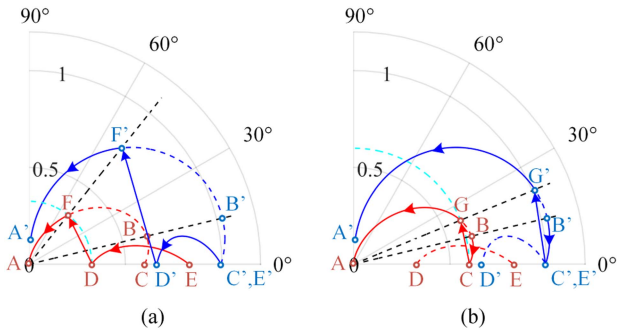

Fig. 10. Two kinds of skip phenomena of PEC. (a) DE segment to AB segment. (b) BC segment to AB segment.

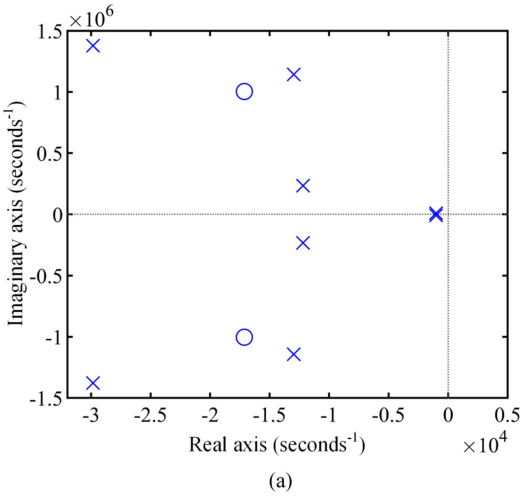

Fig. 11. Pole-zero maps when input and output voltage is 50 V, $R_L = 10\ \Omega$, and $k = 0.4$. (a) VFC. (b) PEC.

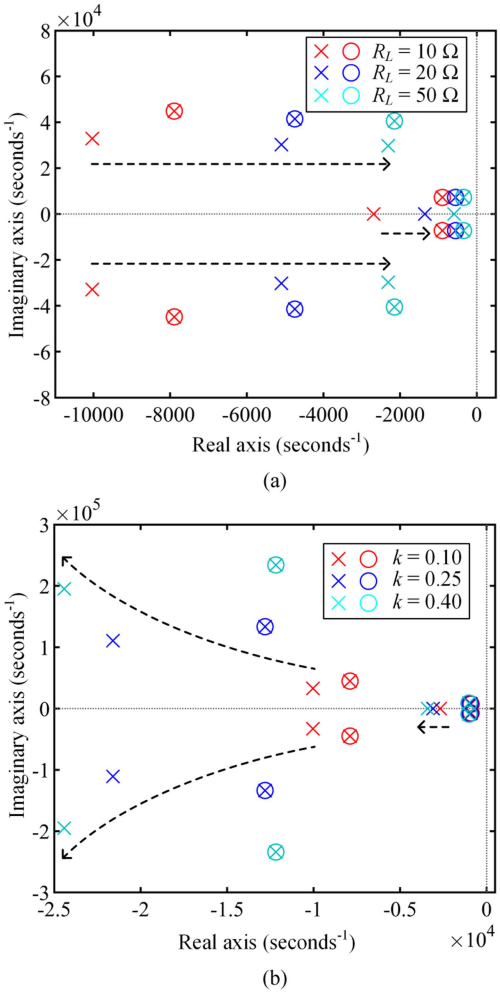

Fig. 12. Pole-zero map when input and output voltage is 50 V. (a) $k = 0.4$ with the load resistor coefficient increasing. (b) $R_L = 10\ \Omega$ with the coupling coefficient increasing.

The effective zone is covered in blue. Obviously, the voltage gain increases monotonically with normalized threshold voltage while the input impedance angle is larger than 0.

2) With Frequency Splitting: When the coupling coefficient increases, there will be two peaks in voltage gain and multiple operating frequencies at which the input impedance angle equals zero, as shown in Figs. 5 and 6. It means that the operating frequency and voltage gain are nonmonotonic. However, traditional control methods, such as proportional-integral-derivative control, require the system to work in the monotonic region. PEC can overcome the nonmonotonicity problem caused by frequency splitting. The polar plot of the input impedance angle with respect to the voltage gain and normalized threshold voltage u_{thn} with $k = 0.4$ can be drawn utilizing the EDF model, as shown in Fig. 9. A-E are five key points at the normalized threshold voltage curve, and A'-E' are five key points at the voltage gain curve. A and A' have the same input impedance angle, which is also suitable for other letters. In addition, C' and E' are close, but they are not the same. In the effective zone where the input impedance angle is larger than 0, curves of voltage gain and normalized threshold voltage are split into two segments, A-C and D-E.

From point D to E, u_{thn} increases; meanwhile, the voltage gain also increases (from D' to E'). For another segment, although the threshold voltage changes continuously from point A to C, u_{thn} increases from point A to B and decreases from point B to C. Similarly, the voltage gain increases from point A' to B', and decreases from point B' to C'. To sum up, the voltage gain also increases monotonically with normalized threshold voltage for the system with frequency splitting.

Another question that should be followed is that the threshold voltage is not continuous; the operation point might skip from one segment to another segment. Fig. 10 illustrates two possibilities for the skip phenomena of PEC. Since the whole system is passive, the input impedance angle is between $-90°$ and $+90°$. Moreover, the input impedance angle is larger than 0 due to the driving circuit of PEC. As a result, only a quarter of the polar plots are diagramed in Fig. 10. Point A is infinitely close to the origin if the input impedance approaches $+90°$. Since DE and BC segments are truncated by the 0-degree line, they will skip to the AB segment if the normalized threshold voltage continues to decline. Nevertheless, the conclusion that the voltage gain increases monotonically with normalized threshold voltage is still effective. This feature is summarized as piecewise monotonic.

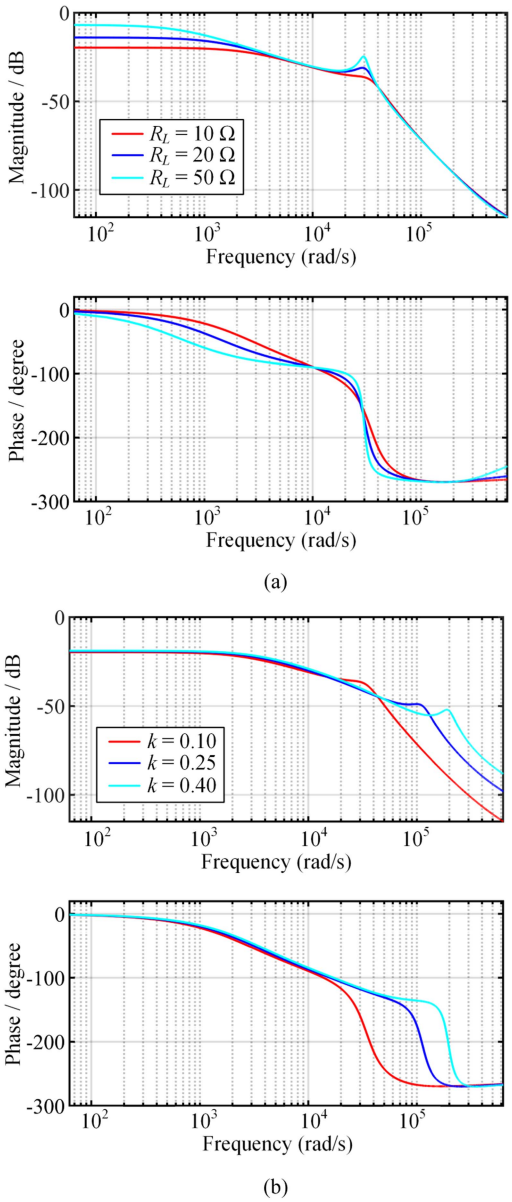

Fig. 13. Bode plot of PEC of the SS-compensated WPT system, $U_{\text{in}} = 50$ V, and $u_o = 50$ V. (a) Multiple load resistors, $k = 0.1$. (b) Multiple coupling coefficients, $R_L = 10\ \Omega$.

C. Small Signal Analysis

Frequent response is important for the closed-loop design. The small signal model of PEC has been derived by utilizing the model of VFC in Section III. Based on the transfer functions of VFC and PEC, the locations of poles and zeros can be watched. The pole-zero maps of these two control methods with the same working conditions are shown in Fig. 11. Only low-frequency poles and zeros are illustrated because the EDF model is not accurate at too high frequencies. It can be seen that pole-zero cancellation occurs in PEC (the area circled in red). As a result, the dominant poles are farther from the imaginary axis, which is beneficial to improve system stability.

In addition, the frequency response of PEC in two conditions, different equivalent load resistors and different coupling coefficients with the same output voltage, is illustrated, as shown in Fig. 12, where arrows indicate the direction of increasing coupling coefficient or load resistors. When the load resistor increases, the dominant poles move toward the imaginary axis. However, when the coupling coefficient increases, the dominant poles move away from the imaginary axis. Meanwhile, these features can also be reflected in bode plots. The low-frequency gain grows with the load resistor increasing, as shown in Fig. 13(a). Whereas it changes little with different coupling coefficients, as shown in Fig. 13(b). The magnitude and phase of the transfer function are related to the locations of poles and zeros. Also, the differences between small signal models of VFC and PEC are distinguished by the different locations of zeros and poles.

Zeros and poles analysis and bode plot are two common tools of the small signal analysis, which help to research the system's important characteristics, such as gain, bandwidth, stability, and distortion, and they are crucial for designing a system to meet specific performance requirements. Furthermore, it enables the evaluation and comparison of various circuit topologies, component values, and parameters to achieve desired performance. The stability analysis and controller optimization can be researched further in detail based on the established small signal model by the EDF approach.

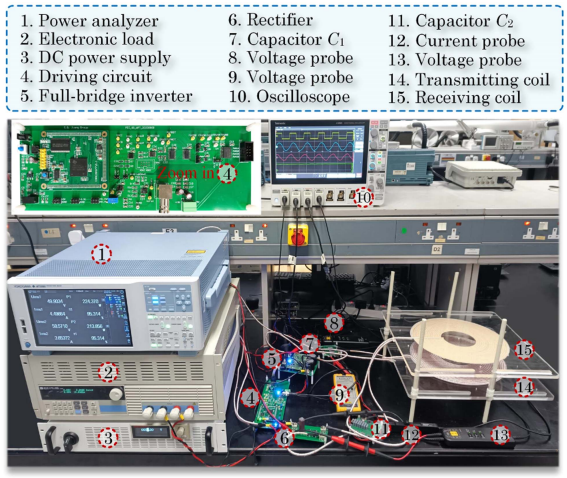

Fig. 14. Experimental setup of PEC for the SS-compensated WPT system.

V. Simulations and Experiments

Simulation in MATLAB/Simulink and experiments are conducted to verify the EDF model and the characteristics of PEC. The system parameters are shown in Table I. The coupling coefficient is changed by adjusting the vertical distance of the coil, and two input voltages, 30 or 50 V, are selected to limit the capacitor voltage u_1, thus protecting the digital controllers. The experimental setup is shown in Fig. 14, and the scheme of the driving circuit is shown in Fig. 15. The AND gates and OR gates are used to switch the control strategy between PEC and VFC, and the signals FlagF and FlagP generate opposite levels to ensure VFC or PEC work. As for VFC, FlagF is high level, and FlagP is low level; the driving signals of the inverter are generated by the ePWM module of DSP, and the switching frequency is determined by the code. And when FlagF is low level, and FlagP is high level, the driving signals of the inverter are generated by PEC. The reason for using VFC is that any

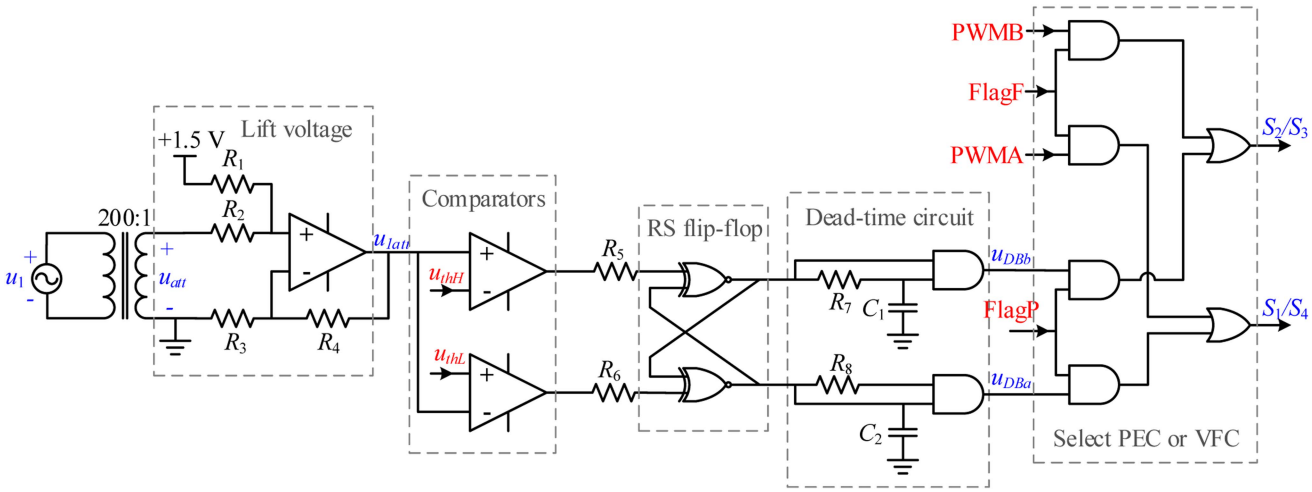

Fig. 15. Driving circuit of PEC in the SS-compensated WPT system. (Note: The signals with red letters are generated by DSP.)

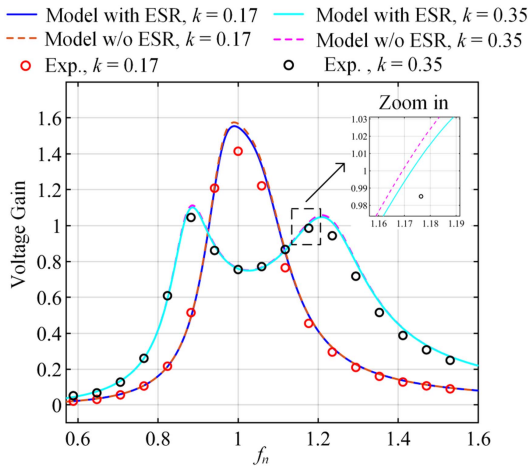

Fig. 16. Voltage gain of the SS-compensated by the EDF model and experiments with different coupling coefficients, $R_L = 10\ \Omega$.

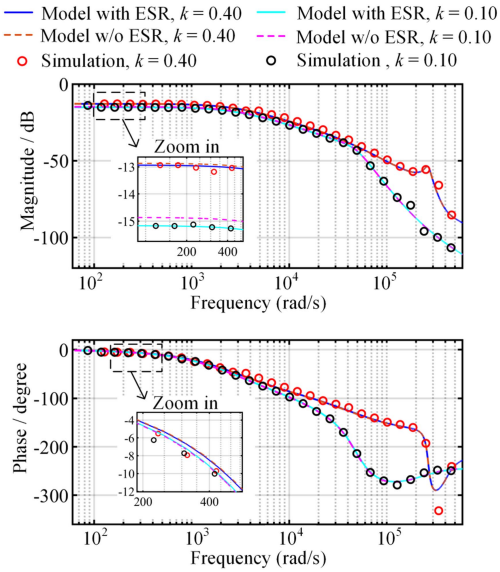

Fig. 17. Frequency response of PEC by EDF model and MATLAB/ Simulink, $k = 0.4$ or 0.1, $U_{\rm in} = 50$ V, $U_o = 30$ V.

TABLE I
PARAMETERS OF EXPERIMENTAL SETUP

Symbol	Quantity	Value
L_1	Primary self-inductance	56.67 µH
L_2	Secondary self-inductance	57.23 µH
C_1	Primary compensation capacitor	61.5 nF
C_2	Secondary compensation capacitor	60.9 nF
C_f	Output filter capacitor	120 µF
k	Coupling coefficient	0.17 or 0.35
U_{in}	Input voltage	30 or 50 V
U_o	Output voltage	~ 50 V
f_0	Nominal resonant frequency	85 kHz
R_1	ESR on the primary side	42.8 mΩ
R_2	ESR on the secondary side	39.2 mΩ
R_L	Load resistor	5-50 Ω
D_i	Inner diameter of the coils	10 cm
D_o	Outer diameter of the coils	28 cm
H	Vertical distance of coils	6 or 11 cm

switching frequency can be enforced. Therefore, the VFC can offer an initial state for PEC to verify the skipping frequency phenomenon of PEC.

The EDF model of PEC is verified first. Two different coupling coefficients are tuned by changing the distance between the transmitting and receiving coils. The results of the large signal model and experiments are consistent, as shown in Fig. 16. The voltage gain calculated by the EDF model with ESRs is closer to the experimental results, and the larger the voltage gain, the more obvious the error of the model without ESRs is. The deviations between the model and experiments are due to the modeling process idealizing the switching devices, like diodes of the rectifier whose forward voltage varies with the current. The frequency response of PEC can be obtained by the tool "model linearizer" of MATLAB (2022b)/Simulink. The model and simulation results exhibit a high level of agreement, as shown in Fig. 17. However, the ESR has a bigger impact on the magnitude than on the phase, and the model with ESR has a higher accuracy than the model without ESR. To sum up,

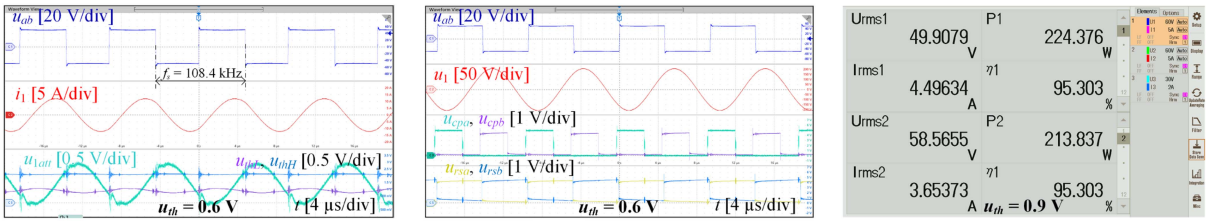

(a) (b) (c)

Fig. 18. Steady-state waveforms of PEC, $k = 0.35$, $U_{\text{in}} = 50$ V. (a) Output voltage and current of the inverter, sensed u_1, u_{thL}, and u_{thH}, $u_{th} = 0.6$ V, $R_L = 10\ \Omega$. (b) Signals of the driving circuit, $u_{th} = 0.6$ V, $R_L = 10\ \Omega$. (c) Measured system efficiency, $u_{th} = 0.9$ V, $R_L = 16\ \Omega$.

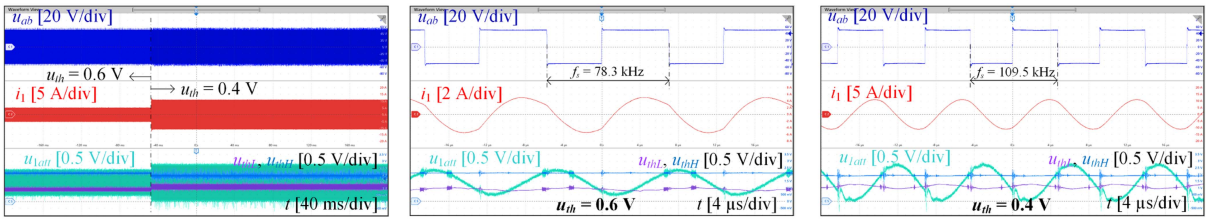

(a) (b) (c)

Fig. 19. Waveforms when $k = 0.35$, $U_{in} = 50$ V, $R_L = 5\ \Omega$. (a) u_{th} stepping from 0.6 to 0.4 V. (b) Zoom in when $u_{th} = 0.6$ V. (c) Zoom in when $u_{th} = 0.4$ V.

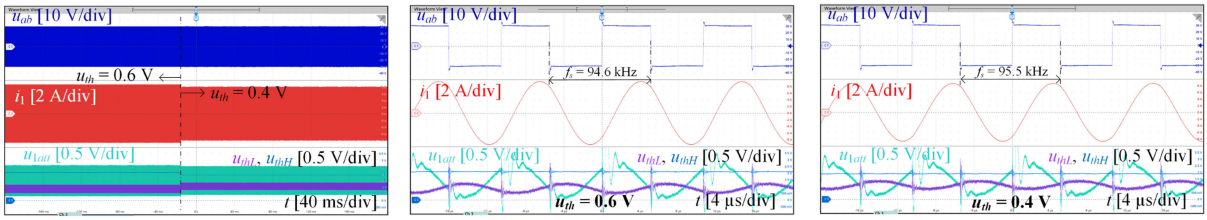

(a) (b) (c)

Fig. 20. Waveforms when $k = 0.17$, $U_{in} = 30$ V, $R_L = 5\ \Omega$. (a) u_{th} stepping from 0.6 to 0.4 V. (b) Zoom in when $u_{th} = 0.6$ V. (c) Zoom in when $u_{th} = 0.4$ V.

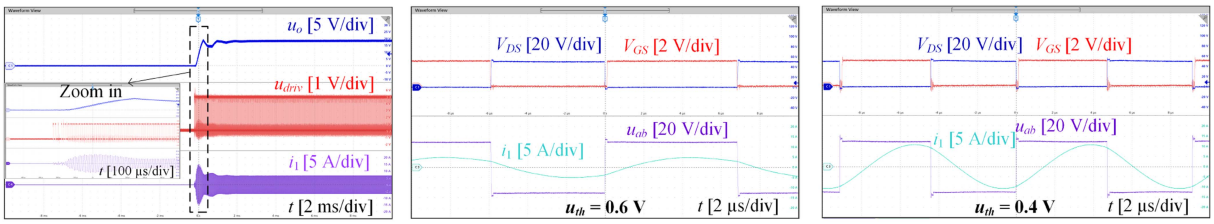

(a) (b) (c)

Fig. 21. Waveforms when $k = 0.35$, $R_L = 5\ \Omega$. (a) Startup process, $U_{\text{in}} = 30$ V. (b) ZVS operation of S_1 when $u_{th} = 0.6$ V, $U_{\text{in}} = 50$ V. (c) ZVS operation of S_1 when $u_{th} = 0.4$ V, $U_{\text{in}} = 50$ V.

the large signal model and small signal model of PEC for the SS-compensated WPT system are effective with high accuracy, and the model with ESRs is more accurate than the model without ESRs.

The characteristics, including ZVS and piecewise monotonic, are demonstrated by experiments. The multiple signals of the driving circuit in a steady state are illustrated in Fig. 18(a) and (b). Specifically, u_{thH} and u_{thL} are two threshold voltages corresponding to U_{1_PN} and U_{1_NP} in (4), and their average value is 1.5 V. $u_{1\,att}$ is the signal after u_1 is attenuated 200 times and then raised by 1.5 V. u_{th} is the distance from u_{thH} or u_{thL} to dc bias 1.5 V, i.e., $u_{th} = (u_{thH}\text{-}u_{thL})/2$. u_{cpa} and u_{cpb} are the outputs of two comparators, and u_{rsa} and u_{rsb} are the outputs of the RS flip–flop. In addition, the dc–dc system efficiency can be up to 95.3% when $u_{th} = 0.9$ V and $R_L = 16\ \Omega$, as shown in Fig. 18(c). In addition, there are two segmented working zones for a large coupling coefficient due to frequency splitting, as illustrated in Fig. 10. The threshold voltage stepping from 0.6 to 0.4 V is demonstrated in Fig. 19(a), and waveforms before and after stepping are enlarged in Fig. 19(b) and (c). It can be found that the switching frequency is changed from 78.3 to 109.5 kHz, and the nominal resonant frequency of 85 kHz is skipped. The experiment proves that the system moves from the DE segment to the AB segment, which is consistent with the analysis in Section IV-B. Compared with Figs. 18(a) and 19(b), their switching frequencies are different, although they

APPENDIX

$$A_{ss}=\begin{bmatrix} 1 & M/L_2 & R_1 & M(R_2+R_e)/L_2 & 0 & 0 & -\Omega L_{eq2} & 0 \\ 1 & L_1/M & R_1 & L_1(R_2+R_e)/M & 0 & 0 & 0 & -\Omega L_{eqm} \\ 0 & 0 & 1 & 0 & \Omega C_1 & 0 & 0 & 0 \\ 0 & 0 & 0 & 1 & 0 & \Omega C_2 & 0 & 0 \\ 0 & 0 & \Omega L_{eq2} & 0 & 1 & M/L_2 & R_1 & M(R_2+R_e)/L_2 \\ 0 & 0 & 0 & \Omega L_{eqm} & 1 & L_1/M & R_1 & L_1(R_2+R_e)/M \\ -\Omega C_1 & 0 & 0 & 0 & 0 & 0 & 1 & 0 \\ 0 & -\Omega C_2 & 0 & 0 & 0 & 0 & 0 & 1 \end{bmatrix}$$

$$B_{ss}=\begin{bmatrix} U_e & U_e & 0 & 0 & 0 & 0 & 0 & 0 \end{bmatrix}^T$$

$$L_{eq1}=\left(L_1L_2-M^2\right)/L_1, L_{eq2}=\left(L_1L_2-M^2\right)/L_2, L_{eqm}=\left(L_1L_2-M^2\right)/M, \Omega=2\pi f_s, R_e=8R_L/\pi^2, U_e=4U_{in}/\pi$$

$$A=\begin{bmatrix} -R_1/L_{eq2} & \Omega & -P_{1c} & P_2 & -1/L_{eq2} & 0 & -1/L_{eqm} & 0 & -P_{3s} \\ -\Omega & -R_1/L_{eq2} & P_2 & -P_{1s} & 0 & -1/L_{eq2} & 0 & -1/L_{eqm} & -P_{3c} \\ -R_1/L_{eqm} & 0 & -P_{4c} & \Omega+P_5 & -1/L_{eqm} & 0 & -1/L_{eq1} & 0 & -P_{6s} \\ 0 & -R_1/L_{eqm} & -\Omega+P_5 & -P_{4s} & 0 & -1/L_{eqm} & 0 & -1/L_{eq1} & -P_{6c} \\ 1/C_1 & 0 & 0 & 0 & 0 & \Omega & 0 & 0 & 0 \\ 0 & 1/C_1 & 0 & 0 & -\Omega & 0 & 0 & 0 & 0 \\ 0 & 0 & 1/C_2 & 0 & 0 & 0 & 0 & \Omega & 0 \\ 0 & 0 & 0 & 1/C_2 & 0 & 0 & -\Omega & 0 & 0 \\ 0 & 0 & P_{7s} & P_{7c} & 0 & 0 & 0 & 0 & -P_8 \end{bmatrix}$$

$$B=\begin{bmatrix} I_{1c}-I_{1s}I_{2c}-I_{2s}U_{1c}-U_{1s}U_{2c}-U_{2s}0 \end{bmatrix}^T$$

$$C=\begin{bmatrix} 0 & 0 & P_{9s} & P_{9c} & 0 & 0 & 0 & 0 & P_{10} \end{bmatrix}$$

$$P_{1s}=\left[4I_{2s}^2U_f/\left(\pi I_{2pk}^3\right)+R_2\right]/L_{eqm}, P_{1c}=\left[4I_{2c}^2U_f/\left(\pi I_{2pk}^3\right)+R_2\right]/L_{eqm}, P_2=4I_{2s}I_{2c}U_f/\left(\pi L_{eqm}I_{2pk}^3\right), P_{3s}=4I_{2s}/(\pi L_{eqm}I_{2pk})$$

$$P_{3c}=4I_{2c}/(\pi L_{eqm}I_{2pk}), P_{4s}=\left(4I_{2s}^2U_f/\left(\pi I_{2pk}^3\right)+R_2\right)/L_{eq1}, P_{4c}=\left(4I_{2c}^2U_f/\left(\pi I_{2pk}^3\right)+R_2\right)/L_{eq1}, P_5=2I_{2s}I_{2c}U_f/\left(\pi L_{eq1}I_{2pk}^3\right)$$

$$P_{6s}=4I_{2s}/(\pi L_{eq1}I_{2pk}), P_{6c}=4I_{2c}/(\pi L_{eq1}I_{2pk}), P_{7s}=2R_LI_{2s}/[\pi C_f(R_L+R_f)I_{2pk}], P_{7c}=2R_LI_{2c}/[\pi C_f(R_L+R_f)I_{2pk}]$$

$$P_8=1/[C_f\,(R_L+R_f)], P_{9s}=2R_LR_fI_{2s}/[\pi(R_L+R_f)I_{2pk}], P_{9c}=2R_LR_fI_{2c}/[\pi(R_L+R_f)I_{2pk}], P_{10}=R_L/(R_L+R_f)$$

have the same threshold voltages, which can also prove there are two segmented zones for PEC with large coupling coefficients. Similarly, a small coupling coefficient is also demonstrated, as shown in Fig. 20. The threshold voltage steps from 0.6 to 0.4 V, and the switching frequency is changed from 94.6 to 95.5 kHz, both larger than the nominal resonant frequency. The system without frequency splitting for a small coupling coefficient works well during the continuous zone when using PEC.

In addition, the driving signals of the inverter rely on the comparison results of $u_{1\,att}$, u_{thL}, and u_{thH}, as shown in Fig. 7. However, $u_{1\,att}$ is so small that the comparators' outputs are both zero during the system startup process. To solve this problem, u_{thL} and u_{thH} are assigned high and low levels together alternately through DSP control with the nominal resonant frequency during the startup process. As shown in Fig. 21(a), the first three cycles are generated by changing u_{thL} and u_{thH}, and the energy flowing into the resonant network supports the system entering the steady state.

Moreover, the inverter's current phase always lags the voltage phase, which can be observed in all experimental waveforms. The results are consistent with the analysis in Section IV-A. This feature is suitable for ZVS operations. More detailed waveforms are shown in Fig. 21(b) and (c), which correspond to the working conditions in Fig. 19(b) and (c). It can be found that V_{DS} is decreased to zero before the switch S_1 turns ON, i.e., V_{GS} is 5 V,

VI. CONCLUSION

Previous studies have demonstrated the good dynamic performance of PEC, but its internal mechanism remains unclear. This article establishes the EDF model of PEC in the SS-compensated WPT system, which is verified to have high accuracy and is used to analyze the characteristics of PEC. The study reveals that the driving circuit causes a phase lag between the inverter's output current and voltage, favoring ZVS operation during the full-load range. Furthermore, when the system has frequency splitting, the working zones of PEC are discontinuous. Nevertheless, regardless of the coupling coefficients being large or small, PEC exhibits the piecewise monotonic property, supporting the design of a unified controller. Experimental results corroborate the characteristics of PEC derived from the mathematical model.

REFERENCES

[1] Y. Liu, U. K. Madawala, R. Mai, and Z. He, "Zero-phase-angle controlled bidirectional wireless EV charging systems for large coil misalignments," *IEEE Trans. Power Electron.*, vol. 35, no. 5, pp. 5343–5353, May 2020.

[2] C. Cai, J. Wang, H. Nie, P. Zhang, Z. Lin, and Y.-G. Zhou, "Effective-configuration WPT systems for drones charging area extension featuring quasi-uniform magnetic coupling," *IEEE Trans. Transp. Electrific.*, vol. 6, no. 3, pp. 920–934, Sep. 2020.

[3] M. Tamura, K. Murai, and M. Matsumoto, "Design of conductive coupler for underwater wireless power and data transfer," *IEEE Trans. Microw.*

[4] A. Babaki, S. Vaez-Zadeh, A. Zakerian, and G. A. Covic, "Variable-frequency retuned WPT system for power transfer and efficiency improvement in dynamic EV charging with fixed voltage characteristic," *IEEE Trans. Energy Convers.*, vol. 36, no. 3, pp. 2141–2151, Sep. 2021.
[5] Y. Li, J. Hu, F. Chen, Z. Li, Z. He, and R. Mai, "Dual-phase-shift control scheme with current-stress and efficiency optimization for wireless power transfer systems," *IEEE Trans. Circuits Syst. I, Reg. Papers*, vol. 65, no. 9, pp. 3110–3121, Sep. 2018.
[6] H. Li, J. Fang, S. Chen, K. Wang, and Y. Tang, "Pulse density modulation for maximum efficiency point tracking of wireless power transfer systems," *IEEE Trans. Power Electron.*, vol. 33, no. 6, pp. 5492–5501, Jun. 2018.
[7] M. Jiang, C. Chen, S. Jia, and H. Chen, "An asymmetrical pulse width modulation with even harmonic for bidirectional inductive power transfer under light load conditions," *IEEE Trans. Ind. Electron.*, vol. 69, no. 9, pp. 8939–8948, Sep. 2022.
[8] Z. Zhou, L. Zhang, Z. Liu, Q. Chen, R. Long, and H. Su, "Model predictive control for the receiving-side DC–DC converter of dynamic wireless power transfer," *IEEE Trans. Power Electron.*, vol. 35, no. 9, pp. 8985–8997, Sep. 2020.
[9] A. Alkasir, S. E. Abdollahi, S. R. Abdollahi, and P. Wheeler, "Enhancement of dynamic wireless power transfer system by model predictive control," *IET Power Electron.*, vol. 15, no. 1, pp. 67–79, Jan. 2022.
[10] S. Chen, W. Ding, L. Huo, X. Wu, S. Shi, and R. Hu, "Dynamic improvement and efficiency optimization of wireless power transfer systems using improved FCS-MPC and P&O methods," *IEEE Trans. Power Electron.*, vol. 38, no. 11, pp. 14702–14718, Nov. 2023, doi: 10.1109/TPEL.2023.3302614.
[11] I.-W. Iam, Z. Ding, C.-F. Ieong, C.-S. Lam, R. P. Martins, and P.-I. Mak, "Optimal bivariate control strategy of multi-stage constant current charging for IPT-based wireless electric vehicle charging," *IEEE Trans. Transport. Electrifi.*, to be published, doi: 10.1109/TTE.2023.3308937.
[12] H. Li, J. Li, K. Wang, W. Chen, and X. Yang, "A maximum efficiency point tracking control scheme for wireless power transfer systems using magnetic resonant coupling," *IEEE Trans. Power Electron.*, vol. 30, no. 7, pp. 3998–4008, Jul. 2015.
[13] M. Li, J. Deng, D. Chen, W. Wang, and Z. Wang, "Maximum efficiency tracking and ZVS realization for wide output voltage range employing segmented TPS modulation scheme," *IEEE Trans. Veh. Technol.*, vol. 72, no. 10, pp. 12770–12783, Oct. 2023, doi: 10.1109/TVT.2023.3274560.
[14] J. Zhou, G. Guidi, K. Ljøkelsøy, and J. A. Suul, "Evaluation and suppression of oscillations in inductive power transfer systems with constant voltage load and pulse skipping modulation," *IEEE Trans. Power Electron.*, vol. 38, no. 8, pp. 10412–10425, Aug. 2023.
[15] E. S. Lee, Y. H. Sohn, B. G. Choi, S. H. Han, and C. T. Rim, "A Modularized IPT with Magnetic Shielding for a Wide-range Ubiquitous Wi-Power Zone," *IEEE Trans. Power Electron.*, vol. 33, no. 11, pp. 9669–9690, Nov. 2018.
[16] C. T. Rim and C. Mi, "General Unified Dynamic Phasor," in *Wireless Power Transfer For Electric Vehicles and Mobile Devices*. Piscataway, NJ, USA: IEEE, 2017, pp. 129–152.
[17] S. R. Sanders, J. M. Noworolski, X. Z. Liu, and G. C. Verghese, "Generalized averaging method for power conversion circuits," *IEEE Trans. Power Electron.*, vol. 6, no. 2, pp. 251–259, Apr. 1991.
[18] A. P. Hu, "Modeling a contactless power supply using GSSA method," in *Proc. IEEE Int. Conf. Ind. Technol.*, Feb. 2009, pp. 1–6.
[19] Z. U. Zahid et al., "Modeling and control of series–series compensated inductive power transfer system," *IEEE J. Emerg. Sel. Topics Power Electron.*, vol. 3, no. 1, pp. 111–123, Mar. 2015.
[20] C. Cheng, T. Chen, X. Cui, Y. Liu, S. Zhang, and C. Mi, "Harmonic modeling and analysis of series-parallel compensated IPT systems with an inductive filter," *IEEE Trans. Power Electron.*, vol. 38, no. 11, pp. 13405–13414, Nov. 2023, doi: 10.1109/TPEL.2023.3302329.
[21] S. Li, F. Li, R. Zhang, C. Tao, and L. Wang, "Accurate modeling, design and load estimation of LCC-S based WPT system with a wide range of load," *IEEE Trans. Power Electron.*, vol. 38, no. 10, pp. 11763–11775, Oct. 2023, doi: 10.1109/TPEL.2023.3279659.
[22] E. S. Lee, J. S. Choi, H. S. Son, S. H. Han, and C. T. Rim, "Six Degrees of Freedom Wide-range Ubiquitous IPT for IoT by DQ Magnetic Field," *IEEE Trans. Power Electron.*, vol. 32, no. 11, pp. 8258–8276, Nov. 2017.
[23] E. S. Lee, B. G. Choi, J. S. Choi, D. T. Nguyen, and C. T. Rim, "Wide-Range Adaptive IPT Using Dipole-coils with a Reflector by Variable Switched Capacitance," *IEEE Trans. Power Electron.*, vol. 32, no. 10, pp. 8054–8070, Oct. 2017.
[24] J. Tang, S. Dong, C. Cui, and Q. Zhang, "Sampled-data modeling for wireless power transfer systems," *IEEE Trans. Power Electron.*, vol. 35, no. 3, pp. 3173–3182, Mar. 2020.
[25] X. Hu, Y. Wang, T. Ma, S. Lyu, G. Gao, and W. Lei, "Discrete-time modelling and stability analysis of wireless power transfer system," *IET Power Electron*, vol. 14, no. 13, pp. 2260–2277, Oct. 2021.
[26] J. Huang, X. He, P. Huo, and R. Xu, "A hybrid modulation strategy for LCC-LCC compensated bidirectional wireless power transfer system to achieve high efficiency in the whole operating range," *IEEE Trans. Ind. Electron.*, vol. 71, no. 1, pp. 327–337, Jan. 2024.
[27] T. Ma, C. Jiang, J. Xiang, X. Wang, K. T. Chau, and T. Long, "Modeling and analysis of wireless power transfer system via unified full-load discrete-time model," *IEEE Trans. Ind. Electron.*, vol. 70, no. 6, pp. 5626–5636, Jun. 2023.
[28] A. Safaee and K. Woronowicz, "Time-domain analysis of voltage-driven series–series compensated inductive power transfer topology," *IEEE Trans. Power Electron.*, vol. 32, no. 7, pp. 4981–5003, Jul. 2017.
[29] T. Ma, Y. Wang, X. Hu, D. Zhao, Y. Jiang, and C. Jiang, "Periodic energy control for wireless power transfer system," *IEEE Trans. Power Electron.*, vol. 37, no. 4, pp. 3775–3780, Apr. 2022.
[30] R. Huang, B. Zhang, D. Qiu, and Y. Zhang, "Frequency splitting phenomena of magnetic resonant coupling wireless power transfer," *IEEE Trans. Magn.*, vol. 50, no. 11, Nov. 2014, Art. no. 8600204.
[31] E. S. Lee and S. H. Han, "2D Thin Coil Designs of IPT for Wireless Charging of Automated Guided Vehicles," *IEEE J. Emerg. Sel. Topics Power Electron.*, vol. 10, no. 2, pp. 2629–2644, Apr. 2022.

Tianlu Ma (Student Member, IEEE) received the B.Eng. degree in electrical engineering and automation from Jilin University, Changchun, China, in 2018, and the M.Sc. degree in electrical engineering from Xi'an Jiaotong University, Xi'an, China, in 2021. He is currently working toward the Ph.D. degree in electrical engineering with City University of Hong Kong, Hong Kong.

His research interests include wireless power transfer modeling and control, and power electronics.

C. Q. Jiang (Senior Member, IEEE) received the B.Eng. and M.Eng. (first class hons.) degrees in electrical engineering and automation from Wuhan University, Wuhan, China, in 2012 and 2015, respectively, and the Ph.D. degree in electrical and electronic engineering from The University of Hong Kong, Hong Kong, in 2019.

He is currently an Assistant Professor with the Department of Electrical Engineering, Faculty Member with the State Key Laboratory of Terahertz and Millimeter Waves, City University of Hong Kong, Hong Kong. Since 2021, he has also been with Clare Hall, University of Cambridge. From 2019 to 2021, he was a Postdoctoral Research Associate with the University of Cambridge, Cambridge, U.K. In 2019, he was a Visiting Researcher with the Nanyang Technological University, Singapore. His research interests include power electronics, wireless power transfer techniques, electric machines and drives, and electric vehicle technologies.

Dr. Jiang was the recipient of the Winner, CAPE Acorn Blue Sky Research Award with the University of Cambridge and First Prize in the Interdisciplinary Research Competition with the University of Hong Kong. He is currently an Associate Editor for *IET Renewable Power Generation*, and the Guest Editor of Energies and IEEE Open Journal of Vehicular Technology.

Yilin Zhang received the B.Eng. degree in electrical engineering and automation from Xi'an Jiaotong University, Xi'an, China, in 2022, and the M.Sc. degree in electronic information engineering from City University of Hong Kong, Hong Kong, in 2023.

He is currently a Research Assistant with The Hong Kong University of Science and Technology (Guangzhou), Guangzhou, China. His research interests include wireless power transfer techniques, motor drive, and controlling.

Yue Wang (Senior Member, IEEE) received the B.S. degree from Xi'an Jiaotong University, Xi'an, China, in 1993, the M.S. degree from Beijing Jiaotong University, Beijing, China, in 1999, and the Ph.D. degree from Xi'an Jiaotong University, in 2003, all in electrical engineering.

From 1993 to 1996, he was an Electrical Engineer with Xi'an Power Electronics Technology Research Institute. He is currently a Full Professor with the School of Electrical Engineering, Xi'an Jiaotong University. His research interests include renewable energy integration, control and stability analysis of power electronic systems, multilevel converters and HVdc, power quality management, and wireless power transfer.

Yuan Cheng (Member, IEEE) was born in Heilongjiang, China, in 1979. He received the B.S., M.Sc., and Ph.D. degrees in electrical engineering from the Harbin Institute of Technology (HIT), Harbin, China, in 2002, 2004, and 2009, respectively.

From 2009 to 2011, he was a Research Scientist for design and optimization of different series–parallel hybrid electric vehicle powertrains organized by the French EV/HEV research network of MEGEVH. In 2012, he was with the Research and Advanced Engineering Department of Groupe PSA, Vélizy, France, where he was responsible for vehicle electrification and electric machine innovations. Since 2020, he has been with HIT as a Full Professor. His research interests include design and optimization of electric machines, electric drive systems, especially PMSMs, and inverters based on SiC devices.

Shumei Cui was born in Heilongjiang, China, in 1964. She received the Ph.D. degree in electrical engineering from the Harbin Institute of Technology (HIT), Harbin, China, in 1998.

She is currently a Professor with the Department of Electrical Engineering, HIT, where she is also the Dean with the Institute of Electromagnetic and Electronic Technology and the Dean with Electric Vehicle Research Centre. Her current research interests include design and control of micro and special electric machines, electric drive system of electric vehicles, control and simulation of hybrid electric vehicles, and intelligent test and fault diagnostics of electric machines.

Dr. Cui is currently the Vice Director Member of the Micro and Special Electric Machine Committee and the Chinese Institute of Electronics, and a member of the Electric Vehicle Committee and the National Automotive Standardization Technical Committee.